ATM Mutations Associate with Distinct Co-Mutational Patterns and Therapeutic Vulnerabilities in NSCLC

Natalie I. Vokes[1,2], Ana Galan Cobo[3], Margarita Fernandez-Chas[4], David Molkentine[1], Santiago Treviño III[1], Vitaly Druker[4], Yu Qian[1], Sonia Patel[1], Stephanie Schmidt[2], Lingzhi Hong[5], Jeff Lewis[6], Waree Rinsurongkawong[6], Vadeerat Rinsurongkawong[6], J. Jack Lee[6], Marcelo V. Negrao[1], Don L. Gibbons[1], Ara Vaporciyan[7], Xiuning Le[1], Jia Wu[5], Jianjun Zhang[1,2], Una Rigney[4], Sonia Iyer[4], Emma Dean[4], and John V. Heymach[1]

ABSTRACT

Purpose: *Ataxia-telangiectasia mutated* (*ATM*) is the most frequently mutated DNA damage repair gene in non–small cell lung cancer (NSCLC). However, the molecular correlates of *ATM* mutations and their clinical implications have not been fully elucidated.

Experimental Design: Clinicopathologic and genomic data from 26,587 patients with NSCLC from MD Anderson, public databases, and a de-identified nationwide (US-based) NSCLC clinicogenomic database (CGDB) were used to assess the co-mutation landscape, protein expression, and mutational processes in *ATM*-mutant tumors. We used the CGDB to evaluate *ATM*-associated outcomes in patients treated with immune checkpoint inhibitors (ICI) with or without chemotherapy, and assessed the effect of *ATM* loss on STING signaling and chemotherapy sensitivity in preclinical models.

Results: Nonsynonymous mutations in *ATM* were observed in 11.2% of samples (2,980/26,587) and were significantly asso-

ciated with mutations in *KRAS*, but mutually exclusive with *EGFR* (*q* < 0.1). *KRAS* mutational status constrained the *ATM* co-mutation landscape, with strong mutual exclusivity with *TP53* and *KEAP1* within *KRAS*-mutated samples. Those *ATM* mutations that co-occurred with *TP53* were more likely to be missense mutations and associate with high mutational burden, suggestive of non-functional passenger mutations. In the CGDB cohort, dysfunctional *ATM* mutations associated with improved OS only in patients treated with ICI-chemotherapy, and not ICI alone. *In vitro* analyses demonstrated enhanced upregulation of STING signaling in ATM knockout cells with the addition of chemotherapy.

Conclusions: *ATM* mutations define a distinct subset of NSCLC associated with *KRAS* mutations, increased TMB, decreased *TP53* and *EGFR* co-occurrence, and potential increased sensitivity to ICIs in the context of DNA-damaging chemotherapy.

Introduction

Ataxia-telangiectasia mutated (*ATM*) is a serine/threonine protein kinase that plays a key role in response to double-stranded DNA breaks by mediating the repair of DNA damage while activating cell-cycle checkpoints via *TP53* (1, 2). Loss of *ATM* can facilitate oncogenesis, as demonstrated by the association between *ATM* germline mutations

and the Ataxia-telangiectasia syndrome, which includes in its clinical manifestation increased rate of cancers and sensitivity to ionizing radiation (1, 3, 4). Somatic mutations in ATM are also common across cancer types, and in non–small cell lung cancer (NSCLC) they have been observed in approximately 5%–10% of tumors (5, 6), representing the most frequently mutated DNA damage repair (DDR) gene. However, despite their prevalence, the significance of *ATM* mutations in NSCLC, including the *ATM* co-mutation landscape, the effect of *ATM* loss on lung cancer biology, and their therapeutic implications, has not been fully elucidated.

Prior work has focused primarily on the prognostic effects of ATM loss as assessed by protein expression. In one analysis of ATM expression by IHC, 40% of lung adenocarcinomas had decreased ATM protein expression, without any impact on overall survival (OS; ref. 7). In contrast, a later analysis used a more stringent quantitative assay and found deficient ATM protein expression in 20% of tumors, along with an associated decrease in OS and possible increased benefit to adjuvant chemotherapy (8). However, ATM protein expression is not typically assessed in clinical practice; whereas somatic mutations in *ATM* are routinely identified on most targeted next-generation sequencing (NGS) panels, the effect of *ATM* mutations on protein function and expression has been incompletely studied (9, 10), making it difficult to determine which genomic events are likely to have a significant biological impact.

Despite this paucity of functional data, there has been growing interest in *ATM* as a possible therapeutic biomarker in NSCLC. Preclinical work suggested that loss of *ATM* or other DDR genes might associate with a higher likelihood of response to immune

[1]Department of Thoracic and Head and Neck Medical Oncology, The University of Texas MD Anderson Cancer Center, Houston, Texas. [2]Department of Genomic Medicine, The University of Texas MD Anderson Cancer Center, Houston, Texas. [3]Department of Molecular Diagnostics, The University of Texas MD Anderson Cancer Center, Houston, Texas. [4]Oncology R&D, AstraZeneca, Cambridge, United Kingdom. [5]Department of Imaging Physics, The University of Texas MD Anderson Cancer Center, Houston, Texas. [6]Department of Biostatistics, The University of Texas MD Anderson Cancer Center, Houston, Texas. [7]Department of Thoracic and Cardiovascular Surgery, The University of Texas MD Anderson Cancer Center, Houston, Texas.

N.I. Vokes, A. Galan Cobo, and M. Fernandez-Chas contributed equally as co-authors of this article.

Corresponding Authors: Natalie I. Vokes, The University of Texas MD Anderson Cancer Center, 1515 Holcombe Boulevard, Unit 432, Houston, TX 77030. E-mail: nvokes@mdanderson.org; and John V. Heymach, jheymach@mdanderson.org

Translational Relevance

Ataxia-telangiectasia mutated (*ATM*) is the most frequently mutated DNA damage repair gene in lung cancer, but its functional and therapeutic implications are understudied. We determine that *ATM* is frequently co-mutated with *KRAS*, among others, and that *KRAS* affects the pattern of *ATM* co-mutations. *ATM* mutations that co-occur with *TP53* typically arise in *KRAS* wild-type samples, in tumors with high mutation loads, and associate with *ATM* missense mutations of unknown functional significance. These findings suggest that *ATM* loss is not tolerated in the context of *KRAS/TP53* loss, which may delineate a population vulnerable to ATM inhibition. In clinical cohorts, *ATM* associates with overall survival in the context of immunotherapy given with chemotherapy, but not immunotherapy monotherapy. Preclinical models demonstrate upregulation in STING signaling in *ATM*-mutated cell lines only after chemotherapy treatment, suggesting that chemotherapy may enhance immune activation in the context of *ATM* loss.

checkpoint inhibitors (ICI), possibly through the acquisition of more neoantigen-forming mutations or STING-mediated activation of IFN signaling (11–13). However, to-date, clinical data are limited. One retrospective analysis showed that *ATM* with concurrent *TP53* mutations associated with increased tumor mutational burden (TMB) and improved ICI outcomes in the OAK and POPLAR cohorts; however, patients with *ATM* mutation without concurrent *TP53* mutations had similar outcomes as *ATM* wild-type patients (14), and the confounding associations between *ATM*, TMB, *TP53*, and ICI outcomes were not clearly disentangled. Another study aggregated DDR defects and showed an association between mutations in DDR genes, increased TMB, and better ICI outcomes, but the study was not powered to evaluate specific DDR genes individually (15). Finally, a recent multi-institutional study also reported an association between *ATM* mutations and ICI response, but did not adjust for TMB and ICI treatment regimen, nor did it report survival outcomes (16). Beyond ICIs, there are increasing numbers of inhibitors of *ATM* and other DDR genes such as *ATR* under clinical development, either alone or in combination with ICI, and the impact of *ATM* loss in mediating sensitivity to these drugs remains an area of active clinical investigation (17).

Given the growing potential therapeutic importance of *ATM* and the paucity of data regarding its functional and clinical impact, we assembled multiple large molecular cohorts and a retrospective real-world clinical cohort to define the co-mutation landscape of *ATM* mutant tumors and interrogate the hypothesis that *ATM* mutations positively impact ICI sensitivity through STING signaling.

Materials and Methods

Study populations

Genie

Adult patients with molecular profiling by the MSK-IMPACT panel or the Dana-Farber Cancer Institute (DFCI) OncoPanel were downloaded from AACR Project GENIE, v10, 2021 release (ref. 18; https://www.synapse.org/#!Synapse:syn7222066), as these centers use gene panels with the largest number of covered genes. Samples were filtered to include patients with NSCLC, and one sample was selected per patient, prioritizing first biopsy from primary site, followed by

sequencing with the most recent panel and highest number of mutations, concordant with prior reports (19).

Gemini

We queried GEMINI, a University of Texas MD Anderson Cancer Center (MDACC) Lung Cancer Moon Shot funded internal database to identify patients who met the following criteria: (i) diagnosis of pathologically confirmed NSCLC, including adenocarcinoma, squamous cell carcinoma, adenosquamous carcinoma, and NSCLC-not otherwise specified; (ii) panel-based sequencing performed at MDACC. Data collected between 2012 and 2021, when the dataset was locked for analysis, were included. One sample from patients with multiple samples was selected by prioritizing the most complete or newest panel, and the highest number of detected mutations.

TCGA

Adult patients with NSCLC and paired whole-exome sequencing (WES) and RNA-sequencing (RNA-seq) data from The Cancer Genome Atlas (TCGA; Pan-Lung Cancer) were included as a distinct molecular cohort (5, 20). Clinical, mutation, copy number, RNA-seq, and reverse-phase protein array (RPPA) data were downloaded from the cBioPortal for Cancer Genomics (21, 22).

ICON

Tumor and paired uninvolved tissue samples were collected at surgical resection from patients enrolled in the ICON study at MDACC, which enrolled patients from 2016 to 2018, and profiled via WES, RNA-seq, multiplex immunofluorescence (mIF), flow cytometry, and RPPA, as previously described (23–25).

Flatiron health-foundation medicine clinicogenomic database

Real-world clinical data were obtained from the US nationwide de-identified Flatiron Health-Foundation Medicine NSCLC clinicogenomic database (FH-FMI CGDB). The de-identified data originated from approximately 800 US cancer clinics. Retrospective longitudinal clinical data were derived from electronic health record (EHR) data, comprising patient-level structured and unstructured data, curated via technology-enabled abstraction, and were linked to genomic data derived from Foundation Medicine (FMI) comprehensive genomic profiling (CGP) tests in the FH-FMI CGDB by de-identified, deterministic matching (26). The study included patients diagnosed with NSCLC who underwent FMI CGP assessment of *ATM* via the FoundationOne CDx assay. Patients included in the clinical analysis (FH-FMI CGDB Clinical) met the following additional inclusion criteria: Advanced or metastatic stage; first-line treatment from January 2016; treatment with standard-of-care chemotherapy and/or ICI. Patients were excluded if they had received a diagnosis of an additional malignancy or received prior therapy for advanced or metastatic NSCLC.

All institutional studies were approved by the appropriate Institutional Review Boards (IRB) and all patients provided written informed consent. For the FH-FMI CGDB dataset, IRB approval of the study protocol was obtained before study conduct, and included a waiver of informed consent. All studies were conducted in accordance the Declaration of Helsinki and international ethical guidelines.

Molecular profiling

GENIE

The GENIE cohort consists of patients sequenced by the DFCI OncoPanel (27) or the MSK-IMPACT Panel (28), as previously described. OncoPanel includes 275 (v1, 4/2013–07/2014), 302

(v2, 07/2014–09/2016), and 447 (v3, 09/2016-ongoing) genes across 3 versions), including 239 genes that are common across all 3 versions of the panel. The MSKCC-IMPACT panel consists of 341, 410, and 468 genes.

GEMINI

Mutational profiling was performed on formalin-fixed, paraffin-embedded tumor tissue or blood samples as previously described (29, 30). The MD Anderson Molecular Diagnostics Laboratory tissue molecular profiling uses NGS-based analysis to detect mutations in 134 or 146 genes. Sequencing of circulating tumor DNA was performed using the MD Anderson Liquid biopsy panel (70 genes) or the Guardant360 panel (74 genes).

TCGA

TCGA cohorts were sequenced as previously described (5, 20, 28). Z-scored protein expression (RPPA) and mRNA expression values (RNA-seq) were used for analysis. Enrichment analyses were limited to the genes included in the GENIE panels.

ICON

As part of the ICON study, tumor samples underwent RNA-seq, WES, TCR-seq, mIF for immune cells, flow cytometry for immune cells, and RPPA profiling, whereas uninvolved adjacent normal tissue underwent mIF, flow cytometry, and RPPA profiling. Samples were processed and analyzed as previously described (23–25, 31–33). The use of patient data, encompassing both sample profiling data and clinical metadata, was approved by the ICON Oversight Committee. RPKM values in protein-coding genes with >0 expression across samples were used for RNA-seq analysis. Enrichment analyses were limited to the genes included in the GENIE panels.

FH-FMI CGDB

Genomic alterations were identified via CGP of >300 cancer-related genes on FMI's NGS test FoundationOne CDx (34–36).

Mutation and TMB analysis

Mutations were categorized as truncating (nonsense; frameshift insertion or deletions), splice site, inframe insertions or deletions (indels), or missense single-nucleotide variants. All nonsynonymous somatic mutations in *ATM* were considered for the co-mutation analysis. For the real-world outcome analysis, only putatively functional *ATM* mutations were considered, consistent with published data and clinical trial inclusion criteria (ClinicalTrials.gov Identifier: NCT03334617). Specifically, truncating, splice site, and a curated list of functional *ATM* missense/inframe mutations were considered pathogenic (Supplementary Table S1).

TMB was calculated in the GENIE cohort as the sum of the number of nonsynonymous mutations normalized by the length of genome sequenced. Panel lengths for the samples sequenced using the Dana-Farber Cancer Center OncoPanel assay were 0.753334, 0.826167, 1.315078 for versions 1, 2, and 3, respectively; panel lengths for MSK-IMPACT were 0.896665, 1.016478, and 1.1393222 for versions 341, 410, and 468 (37). TMB was not calculated for the GEMINI cohort as the available panels are shorter and not validated for TMB inference (38). TMB in the TCGA was calculated as the sum of nonsynonymous mutations. TMB in the FH-FMI CGDB cohort was calculated via the FoundationOne algorithm, which sums somatic, coding mutations or indels over the length of genome sequenced (38).

PD-L1

PD-L1 in the FH-FMI CGDB cohort was assessed as the laboratory-based report of PD-L1–positive tumor cells, and were grouped into PD-L1 expression <1%, 1%–49%, or ≥50%.

Mutational signature analysis

Mutational signature analysis of the TCGA data was performed using deconstructSigs (39) and Cosmic Mutational Signatures v2, as this is more appropriate for WES data. After initial analysis, signature assignment was limited to Signatures 1, 2, 3, 4, 5, 13, 17, 18, and 28, as these were the most abundant signatures in the dataset.

Clinical endpoints

Retrospective longitudinal clinical data were derived from EHR data, comprising patient-level structured and unstructured data, curated via technology-enabled abstraction, and were linked to genomic data derived from FMI CGP tests in the FH-FMI CGDB by de-identified, deterministic matching (26). Evaluation of real-world OS (rwOS) was defined as the time from the index date until the death date. For patients with no record of death, rwOS was censored at the last activity during the study period. The landmark of rwOS (OS12/OS24/OS36) was also derived from the Kaplan–Meier estimate. Left truncation bias was mitigated using risk set adjustment methods.

Cell culture

The LKR13 murine cell lines were generously provided by Dr. Tyler Jacks (Massachusetts Institute of Technology) in 2005 and were derived by serial passage of minced lung adenocarcinoma tissues from K-ras^{LA1}mice (40). The cells were cultured in RPMI-1640 supplemented with 10% FBS (Invitrogen), 1% Pen–Strep, and 1% L-glutamine (HyClone). Isogenic pair for ATM (KA) were generated using CRISPR/Cas9 system by transfection of pSpCas9(BB)-2A-GFP (PX458) plasmid with specific sgRNA. H2030 and H23 human cell lines were obtained from the ATCC (RRID:CVCL_1547). All cells were maintained in RPMI-1640 medium (Sigma) supplemented with 10% FBS, 1% glutamine, and 1% penicillin–streptomycin. Fingerprinting and *Mycoplasma* test (MycoAlert mycoplasma detection kit) were performed periodically for authentication.

Drugs

Gemcitabine and SN-38 were purchased from Selleck Chemicals. Cisplatin, docetaxel, pemetrexed, and topotecan were generously provided by MD Anderson Cancer Center pharmacy (Houston, TX). Drugs were resuspended and aliquots were stored at −80°C and each aliquot was used only once.

Western blot analysis

Cell pellet was washed with cold PBS once and then lysed with a variable volume of ice-cold lysis RIPA buffer (1% Triton X-100, 50 mml/L HEPES, pH 7.4, 150 mmol/L NaCl, 1.5 mmol/L MgCl$_2$, 1 mmol/L EDTA, 100 mmol/L NaF, 10 mmol/L Na pyrophosphate, 1 mmol/L Na$_3$VO$_4$, 10% glycerol, supplemented immediately before cell lysis with 1 mmol/L phenylmethylsulfonyl fluoride, complete protease inhibitor, and phosSTOP phosphatase inhibitor cocktail; Roche Applied Science (Penzberg, Alemania). Cell lysates were sonicated at 100 amplitude for 2 minutes using a QSonica Q700. Lysates were centrifuged at 14,000 rotations per minute (rpm) for 15 minutes at 4°C, and then the cleared supernatant was collected and protein concentration was quantified using the colorimetric Bio-Rad Protein Assay Dye Reagent Concentration (Bio-Rad), according with the manufacturer's protocol. Next, 20–25 µg of total protein was loaded

and resolved in 4%–20% pre-cast gradient gels (Bio-Rad) and transferred to polyvinylidene difluoride membranes using the Trans-Blot Turbo transfer system and Trans-Blot Turbo RTA transfer kit (Bio-Rad), according to the manufacturer's protocol. Membranes were blocked in 5% nonfat dry milk (Bio-Rad) in 0.1% TBS-Tween (150 mmol/L NaCl, 10 mmol/L Tris-HCL, pH 8) for 1 hour at room temperature and incubated with the following primary antibodies with 0.1% goat serum plus 2 mmol/L EDTA dissolved in 0.1% TBS-Tween: β-Tubulin 1:5,000 (#86298), pTBK1/NAK ser172 1:250 (#5483), TBK1/NAK 1:1,000 (#3504), pIRF3 ser396 1:500 (#29047), IRF3 1:2,000 (#4302), pSTING ser365 1:250 (#72971), STING 1:1,000 (#50494), and cGAS 1:3,333 (#31659), phospho-IRF-3 (Ser396; D6O1M) Rabbit 1:500 (#29047) RRID:AB_1274666, IRF-3 (D6I4C) XP Rabbit 1:1,000 (#11904), phospho-TBK1/NAK (Ser172; D52C2) XP Rabbit 1:500 (#5483), TBK1/NAK (D1B4) Rabbit 1:1,000 (#3504), cGAS (D1D3G) Rabbit 1:1,000 (#15102), STING (D1V5L) Rabbit 1:1,000 (#50494), and β-Actin (8H10D10) Mouse 1,10,000 (#3700) were purchased from Cell Signaling Technology and incubated overnight at 4°C. Membranes were washed briefly with 0.1% TBS-Tween and then incubated with horseradish peroxidase (HRP)–conjugated secondary antibodies at a concentration of 1:2,000 in 5% nonfat dry milk for 1 hour at room temperature. Signal was developed with Radiance plus Femtogram HRP Chemiluminescent Substrate (Azure Biosystems) detection reagents.

IP10 (CXCL10) ELISA

Complete RPMI media were conditioned in LKR13 K or LKR13 KA cells for 48 hours. Conditioned media were removed and stored at −80°C as 1-mL aliquots. The manufacturer's instructions for the Mouse IP-10 ELISA kit (Invitrogen, BMS6018) were followed. Briefly, ELISA strips were pre-washed twice. 100 µL undiluted tissue culture media were added per sample. 50-µL biotin-conjugated antibody was added per well and incubated for 2 hours. Each well was then washed 6 times. 100-µL Streptavidin–HRP was added and incubated for 1 hour while shaking. Each well was again washed 6 times. 100-µL TMB substrate was added for 10 minutes while slowly shaking. 100-µL STOP solution was added and then immediately read absorbancy at 450 nm using a fluorSTAR Optima plate reader (BMG Labtech). All steps and incubations were performed at room temperature.

Quantitative PCR

LKR13 K and LKR13 KA cells were plated into 60-mm dishes for 5 days. Cells were then collected in 350-µL RLT buffer plus 0.1% 2-mercaptoethanol (RNeasy kit, Qiagen, 74104) and passed through a QIAshredder column (Qiagen, 79654). DNA was removed by incubating in 75-µL DNase for 15 minutes at room temperature (DNase set, Qiagen, 79254). RNA was washed then eluted in 30-µL RNase-free water and quantified using DeNovix nanodrop spectrophotometer. All RNA used for qPCR had 260/280 ratios greater than 2.0. 1 µg total RNA was reverse transcribed using iScript reagent (Bio-Rad, 1708891). Gene expression was quantified using TaqMan Fast Advance Master Mix (Applied Biosystems, 4444557, lot 01295842) and TaqMan gene expression systems (Applied BioSystems). Real-time PCR was performed on a 7500 Fast Real-Time PCR System (Applied BioSystems). 50 ng per well of each sample was ran in triplicate and three independent experiments were averaged.

Cell viability assay and IC$_{50}$ value estimation

The IC$_{50}$ value was estimated using the CellTiter-Glo Luminescent cell viability assay (Promega), according to the manufacturer's protocols. When cells were in the exponential growth phase, the cells were detached and counted using a Countess automated cell counter (Invitrogen). An optimized number of viable cells for each cell line were then plated in polybase white 384-well plates (Greiner Bio-One), in triplicate for each experimental condition. Cells were allowed to attach, depending on the cell line, for 24 hours and subsequently exposed to seven different concentrations of indicated drugs (serial 3-fold dilutions) in a final volume of 40 µL of media per well, and plates were then incubated for an additional 96 hours. Next, 11 µL of CellTiter-Glo reagent was added to each well, and contents were briefly mixed and incubated for 5 minutes. Bioluminescence was measured using a FLUOstar OPTIMA multimode microplate reader (BMG LABTECH). Average readings from triplicate wells were then expressed as a percentage of average bioluminescence measured from control DMSO wells treated with vehicle (DMSO) at the highest DMSO concentration in drug-treated cells. A dose–response model was used to estimate IC$_{50}$ values from cell viability data using Graph-Pad Prism software version 8 (RRID:SCR_002798) at 50% of inhibition.

Statistical analysis

Downstream analyses were performed using R version 4.0.3 or GraphPad Prism version 6.00 for Windows (GraphPad Software). Categorical and continuous variables were summarized descriptively using percentages and medians, respectively. Differences between two groups were compared using the Fisher's exact test for categorical variables. The nonparametric Mann–Whitney U and Kruskal–Wallis H tests were used to compare the mean ranks between two groups (U test) or three groups (H test). For parametric data, an unpaired t test was used to compare the mean with two groups, and a one-way ANOVA was used to compare the means of three or more groups. Spearman and Pearson's correlation coefficients were used to assess the association between continuous variables. Fisher's exact test P values and conditional odds ratios were used to assess co-occurrence and mutual exclusivity with nonsynonymous *ATM* mutations. Positive log odds ratios represented a tendency toward co-occurrence and negative log odds ratios represented a tendency toward mutual exclusivity (41). Enrichment analyses were performed individually in each cohort, as well as in aggregate; cohorts were aggregated through meta-analysis, whereby a logistic regression random effects model was fit with both a random and fixed effect for the mutation status of the gene in question. The effect of mutation along with an intercept term was allowed to vary within each database. P values were then calculated using a χ^2 test for the inclusion of that fixed effect against a model that did not include the fixed effect. All P values were two-tailed and for all analyses, a P value of ≤0.05 is considered statistically significant, unless otherwise specified. Correction for multiple hypothesis testing was performed using FDR.

Baseline demographic and disease characteristics in the FH-FMI CGDB cohort were described overall and stratified by ATM status and treatment exposure (ICI, ICI-Chemotherapy, and chemotherapy). Multiple variable adjustment of the FH-FMI cohort KM curves and Cox PH models included age, gender, smoking history, ECOG performance status, histology, TMB, and PD-L1 expression. A stepwise algorithm was used to select from these baseline clinically relevant covariates, with Akaike information criterion as the statistic for feature selection. The possible effect of alterations of interest was identified using ANOVA to compare the stepwise model before and after, including each alteration. Alterations in *ATM*, *TP53*, *KEAP1*, *KRAS*, and *STK11* were considered. The final stepwise model was built, including the features that resulted in the best fit of the survival data.

Data availability

GENIE data are available at https://www.synapse.org/#!Synapse:syn7222066, and TCGA data at https://www.cbioportal.org/ (Pan-Lung Cancer, https://www.cbioportal.org/study/summary?id=nsclc_tcga_broad_2016). The FH-FMI CGDB data used in this study have been originated by Flatiron Health, Inc. Requests for data sharing by license or by permission for the specific purpose of replicating results in this article can be submitted to DataAccess@flatiron.com. MD Anderson data are available from the corresponding author upon reasonable request.

Results

Prevalence of ATM mutations and co-occurrence with other genomic events

To analyze the distribution and co-mutation landscape of *ATM* mutations in NSCLC, we assembled 5 genomic datasets; three large clinicogenomic datasets with clinical panel–based sequencing (GENIE, FH-FMI CGDB, and GEMINI), and two smaller molecular datasets with more extensive molecular profiling, including WES, RNA-seq, and RPPA (TCGA and ICON; **Fig. 1A**; Supplementary Fig. S1A; **Table 1**). Samples with and without nonsynonymous mutations in *ATM* were identified. In total, *ATM* mutations were observed in 2,980/26,587 samples (11.2%). There were no clinicopathologic features that associated with *ATM* alterations in all cohorts, but on meta-analysis, *ATM* mutations associated significantly with tobacco use and adenocarcinoma histology (**Table 1**). *ATM* mutations were distributed throughout the protein structure and were predominantly missense mutations, with a smaller proportion (18.8%–28%) occurring as truncating mutations (**Fig. 1B**; Supplementary Fig. S1B). Co-mutation analyses demonstrated significant enrichment of *KRAS* mutations in *ATM*-mutated (*ATM*-mt) versus wild-type (*ATM*-wt) tumors (FDR $q < 0.0001$; OR, 2.24), and significant de-enrichment of *EGFR* mutations (FDR $q < 0.001$; OR, 0.52), both across cohorts and within the individual cohorts (**Fig. 1C and D**; Supplementary Fig. S2). Multiple other genes, including *STK11*, *ARID1A*, and *RBM10*, were significantly co-mutated with *ATM*; *TP53* was significantly de-enriched in *ATM* mutant tumors in the largest individual cohorts (GENIE, FH-FMI CGDB, and GEMINI), but was not significant in the meta-analysis (OR, 0.68; $q = 0.24$; **Fig. 1C**; Supplementary Fig. S2; Supplementary Table S2),

KRAS mutation status constrains the ATM co-mutation landscape

Given the significant co-occurrence between *ATM* and *KRAS* mutations and known patterns of co-mutation within *KRAS* mutant NSCLC (42–44), we next investigated whether *ATM* co-mutation patterns differed in a *KRAS*-mutated (*KRAS*-mt) versus wild-type (*KRAS*-wt) context. Within *KRAS*-mt tumors, we observed that *ATM* mutations were significantly less likely to co-occur with *TP53* or *KEAP1* mutations, both on meta-analysis and within cohorts (**Fig. 2A and B**; Supplementary Fig. S3). However, despite the expected frequent co-occurrence between *KEAP1* and *STK11* mutations (42, 43) in the *KRAS*-mt tumors, *ATM* was mutually exclusive specifically with *KEAP1*, without any observed differential frequency of *STK11* loss in *ATM*-mt versus *ATM*-wt (**Figs. 2A** and **B**, and **1C**; Supplementary Table S3).

Conversely, in *KRAS*-wt samples, *ATM* was significantly co-mutated with both *STK11* and *KEAP1*, along with a number of epigenetic modifiers, including SWI/SNF complex genes (*ARID2*, *ARID1A*, and *ARID1B*; **Fig. 2A and C**). In the *KRAS*-wt context there

was no significant de-enrichment of *TP53*, but *EGFR* alterations were less likely to co-occur with *ATM*, indicating that the de-enrichment for *EGFR* mutations in the overall analysis (**Fig. 1C**; Supplementary Fig. S2A–S2D) was not driven by the mutual exclusivity between *KRAS* and *EGFR*, but rather specific to *ATM* itself (Supplementary Table S4).

Given the striking differential *TP53* mutation patterns, we assessed whether *ATM* mutations differ in *TP53* mutant versus wild-type contexts, and observed an enrichment for *ATM* missense rather than truncating mutations in *TP53*-mutated tumors (**Fig. 2D**, $P < 2.2e-16$), arising specifically in the *KRAS*-wt/*TP53*-mutated tumors (Supplementary Fig. S4A). To infer whether these differences associated with differential impact on *ATM* function, we examined the association between ATM protein expression and *ATM* mutation class, and observed reduced expression by RPPA in samples with truncating rather than missense mutations (**Fig. 2E**), though the sample size was modest. The association between *ATM* mutation class and *ATM* mRNA expression was less pronounced (Supplementary Fig. S4B), and there was only a weak correlation between ATM protein and *ATM* mRNA expression ($R = 0.23$–0.36; Supplementary Fig. S4C and S4D), indicating that *ATM* mRNA expression is likely a weak surrogate for ATM protein expression. These results are concordant with a recent publication demonstrating no loss of ATM protein expression in the context of concurrent *TP53* mutations (45), consistent with the hypothesis that *ATM* missense mutations that co-occur in the *TP53* mutant context may be passenger mutations with unclear functional significance.

ATM mutation associates with a higher mutational burden driven by distinct mutational processes in KRAS-mt versus Wt contexts

Given the association between *ATM* and DNA damage repair, we next sought to understand whether *ATM* mutations associate with distinct mutational processes. In the GENIE (**Fig. 3A**; Supplementary Fig. S5A and S5B), FH-FMI CGDB and TCGA cohorts (Supplementary Fig. S5C and S5D), we observed a higher TMB in *ATM*-mt versus wt tumors. This increase in TMB was most pronounced in the *ATM*-mt, *KRAS*-wt tumors (**Fig. 3B**; Supplementary Fig. S5E and S5F), and within this group, *TP53*-mutated tumors had markedly higher TMB (**Figs. 3C** and **1D**), consistent with high acquisition of somatic passenger mutations in these tumors.

To identify mutational processes giving rise to the increased TMB, mutational signature analysis was performed, focusing on the TCGA due to increased validity of mutational signature calling from WES (Materials and Methods). *ATM*-mt tumors were enriched for signature 4, which arises from tobacco-related mutagenesis, and had markedly lower proportion of signature 5, a pan-cancer aging signature (**Fig. 3D**). Stratification by *ATM*/*KRAS* co-mutation status demonstrated that this mutational pattern was consistent with *KRAS* mutant tumors more generally rather than *ATM*-mutated tumors more specifically; within *KRAS*-mutated or wild-type tumors there was no difference in mutational signature proportion by *ATM* mutation status (**Fig. 3E**). Taken together, this suggests that the mutational processes giving rise to increased TMB in *ATM*-mutated tumors is driven more by the processes driving oncogenesis in *KRAS*-mt versus wt tumors, respectively, rather than being unique to *ATM* loss.

ATM alterations associated with sensitivity to ICI with chemotherapy but not ICI monotherapy

Given prior reports linking *ATM* mutations with ICI response, we next investigated the clinical implications of *ATM* mutation by
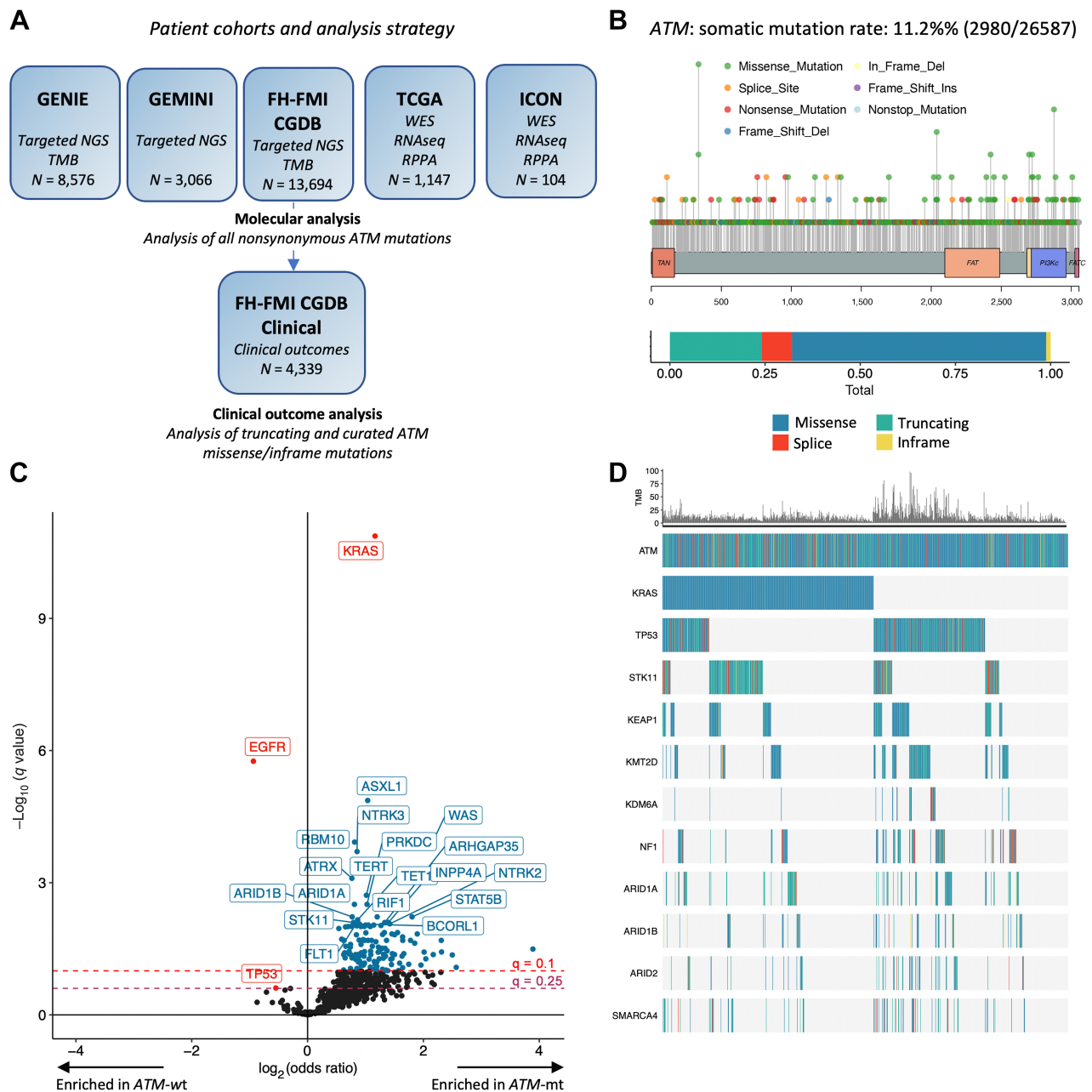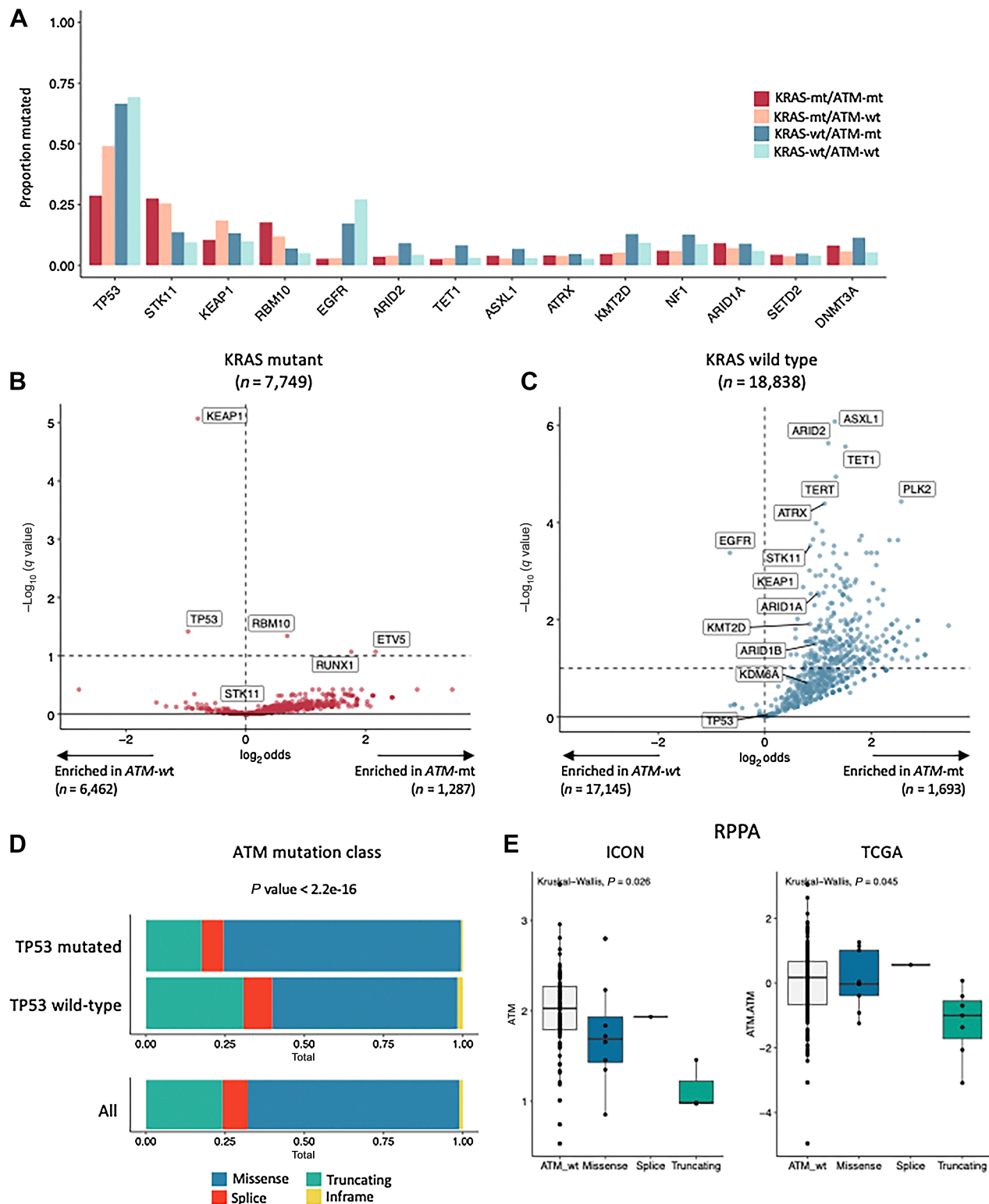
Figure 1.
Genomic landscape of *ATM* mutations in non–small cell lung cancer. **A,** Molecular cohorts and clinical sub-cohort used for analysis, along with the definition of *ATM* mutations used in the molecular and clinical analyses, respectively. **B,** Lollipop plot of *ATM* mutations, along with the distribution of mutation types within *ATM*. **C,** Enrichment analysis depicting genes more likely to be co-mutated with *ATM* (positive log odds ratio, *x*-axis) or mutually exclusive with *ATM* (negative log odds ratio) across all five molecular cohorts. The *y*-axis depicts negative log of the FDR-corrected *P* value. **D,** Representative co-mutation plot from the GENIE cohort to visualize *ATM* mutations, most frequently co-occurring mutations, and tumor mutational burden (TMB; *n* = 809 samples with *ATM* mutations). *ATM*-mt = *ATM* mutated, *ATM*-wt = *ATM* wild-type. Dashed maroon line represents *q* = 0.25 and dashed red line represents *q* = 0.1. *KRAS*, *EGFR*, and *TP53* highlighted in red.

assessing whether *ATM* loss associated with differential outcomes to ICIs. Given the findings above, we focused our clinical analysis on likely functional *ATM* mutation events by applying selection criteria used in current ongoing clinical trials, which define functional *ATM* mutations as truncating, splice site, or a curated list of missense/inframe mutations (Supplementary Table S1); missense mutations outside this curated list were considered non-functional. For the clinical outcome analysis, we used patients from the FH-FMI CGDB dataset who had been treated with systemic therapy for advanced or metastatic disease. After applying exclusion criteria (Supplementary Fig. S1A; Materials and Methods), 4,339 patients with NGS profiling were included (Supplementary Table S5). Compared with all

Table 1. Clinical characteristics of the five molecular cohorts, stratified by ATM mutation status.

	AACR GENIE (n = 8,576)			FH-FMI CGDB (n = 13,694)			GEMINI (n = 3,066)			TCGA (n = 1,147)			ICON (n = 104)			Meta-analysis q value
	ATM mut (%)	ATM WT (%)	P	ATM mut (%)	ATM WT (%)	P	ATM mut (%)	ATM WT (%)	P	ATM mut (%)	ATM WT (%)	P	ATM mut (%)	ATM WT (%)	P	
All	807 (9.4)	7,769 (90.6)		1,895 (13.8)	11,799 (86.2)		179 (5.8)	2,887 (94.2)		88 (7.7)	1,059 (92.3)		11 (10.6)	93 (89.4)		0.858586
Age at Dx			0.183			<0.001			0.296			0.0417			0.8199	
Median, y, range	68.0 (26.0–88.0)	68.0 (19.0–88.0)		69.00 (23.00–85.00)	68.00 (24.00–85.00)		65.6 (35.3–86.4)	64.3 (24.5–92.1)		66.0 (40.0–83.0)	67.5 (38.0–90.0)		66.0 (45.0–85.0)	68.0 (38.0–85.0)		
Gender			0.4981			0.893			0.638			0.461			0.341	
Male	321 (39.9)	3,194 (41.2)		935 (49.3)	5,845 (49.5)		91 (50.0)	1,382 (47.8)		48 (54.5)	625 (59.2)		7 (63.6)	42 (45.2)		
Female	483 (60.1)	4,563 (58.8)		960 (50.7)	5,954 (50.5)		88 (50.0)	1,505 (52.2)		40 (45.5)	431 (40.8)		4 (36.4)	51 (54.8)		
Tobacco use						<0.001			0.00291			0.2296			0.206	**4.24E−09**
Never				170 (9.0)	1,990 (16.9)		29 (16.2)	779 (27.0)		4 (4.5)	108 (10.2)		0 (0.0)	19 (20.4)		
Current/Former				1,721 (90.8)	9,775 (82.8)		143 (69.8)	1,973 (68.3)		70 (79.5)	822 (77.6)		11 (100)	74 (79.6)		
Unknown				4 (0.2)	34 (0.3)		7 (3.9)	135 (4.6)		14 (15.9)	129 (12.2)		0 (0.0)	0 (0.0)		
Histology			0.00074			<0.001			0.307			0.0433			0.861	**0.045815**
ADC	689 (85.4)	6,368 (82)		1,473 (77.7)	8,502 (72.1)		140 (78.2)	2,382 (82.5)		60 (68.2)	603 (56.9)		9 (81.8)	64 (68.8)		
SCC	62 (7.7)	927 (11.9)		345 (18.2)	2,787 (23.6)		25 (14.0)	326 (11.3)		28 (31.8)	456 (43.1)		2 (18.2)	23 (24.7)		
Other	56 (6.9)	474 (6.1)		77 (4.1)	510 (4.3)		14 (7.8)	179 (6.2)		0 (0.0)	0 (0.0)		0 (0.0)	6 (6.5)		
Stage at Dx						0.171			0.284			0.372			0.171	0.708
I				233 (12.3)	1,312 (11.1)		39 (21.8)	514 (17.8)		39 (44.3)	538 (50.8)		4 (36.4)	47 (50.5)		
II				138 (7.3)	931 (7.9)		21 (11.7)	271 (9.4)		24 (27.2)	281 (26.5)		7 (63.6)	29 (31.2)		
III				281 (14.8)	1,651 (14.0)		38 (21.2)	633 (21.9)		17 (19.3)	172 (16.2)		0 (0.0)	16 (17.2)		
IV				1,004 (53.0)	6,379 (54.1)		79 (44.1)	1,442 (49.9)		5 (5.7)	33 (3.1)		0 (0.0)	1 (1.1)		
Unknown				239 (12.6)	1,526 (12.9)		2 (1.1)	27 (0.9)		3 (3.4)	35 (3.3)		0 (0.0)	0 (0.0)		

Figure 2.
KRAS constrains the *ATM* co-mutation landscape across molecular cohorts. **A,** Proportion of samples with mutations in the genes indicated on the *x*-axis, stratified by *ATM/KRAS* co-mutation status, proportions aggregated across cohorts. **B** and **C,** Enrichment analysis depicting genes more likely to be co-mutated with *ATM* (positive log odds ratio, *x*-axis) or mutually exclusive with *ATM* (negative log odds ratio) in (**B**) *KRAS*-mutated samples or (**C**) *KRAS* wild-type samples. Data from cohorts aggregated via meta-analysis. **D,** Proportion of *ATM* mutation variant class in *TP53* mutated versus wild-type across all cohorts; variant class across all *ATM* mutations shown below for reference. **E,** ATM protein expression by reverse phase protein array (RPPA) stratified by *ATM* mutation variant class in the ICON and TCGA cohorts.
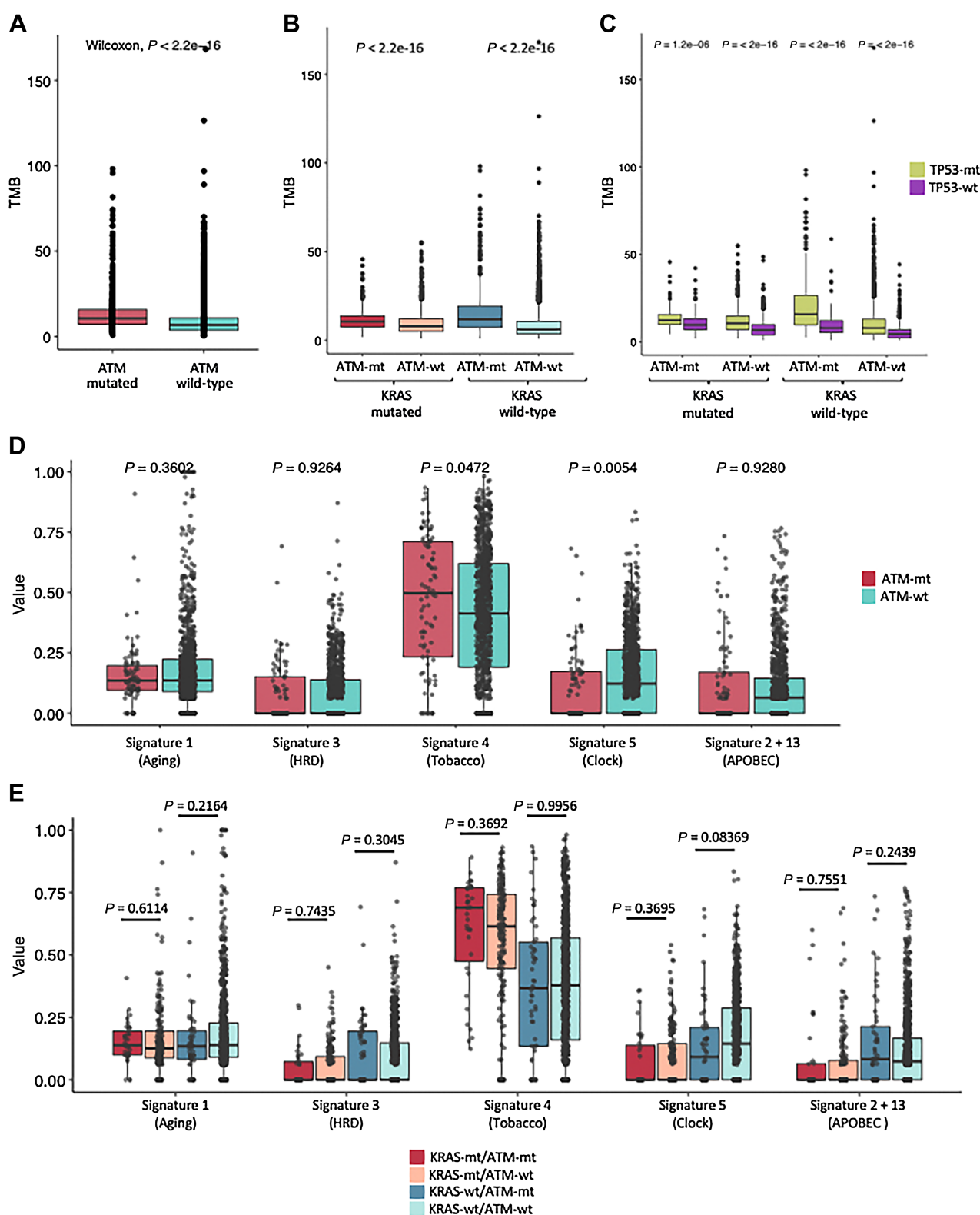
Figure 3.
Genomic features of *ATM* mutant non–small cell lung cancer. Tumor mutational burden (TMB) in the GENIE cohort in (**A**) *ATM*-mutant (*ATM*-mt) versus *ATM* wild-type (*ATM*-wt) samples; **B,** TMB, stratified by *ATM/KRAS* co-mutation status. **C,** TMB stratified by *ATM/KRAS* co-mutation status, further stratified by *TP53* mutation status. **D** and **E,** Mutational signature proportion in the TCGA dataset, stratified by (**D**) *ATM* and (**E**) *ATM/KRAS* mutation status; HRD, homologous repair deficit.

non-synonymous mutations, the selected pathogenic mutations were enriched for truncating and splice events, as expected (Supplementary Fig. S6A).

Pathogenic *ATM* mutations were observed in 238/4,339 (5.5%) patients. Pathogenic *ATM* mutations associated with higher TMB ($P = 0.037$; **Fig. 4A**) but no difference in PD-L1 expression (**Fig. 4B**). Across the whole cohort, we observed improved OS in patients with *ATM*-mt versus wt (**Fig. 4C**). To determine how this association was modified by treatment and confounding variables such as histology, TMB, and smoking status, all of which also associate with ICI outcomes, we stratified the cohort by treatment and performed multivariate adjustment. In the unadjusted analyses, *ATM* mutation associated with improved outcomes to ICI monotherapy (ICI-mono) and ICI combined with chemotherapy (ICI-chemo), but not with chemotherapy alone (Chemo-mono; **Fig. 4D**). However, when included in a multivariate model, *ATM* mutations only associated with improved OS in the context of ICI-chemotherapy treatment (**Fig. 4D** and **E**). To validate these findings through an orthogonal analytic approach, we performed a step-wise feature selection approach, including other genomic events of interest that may also associate with *ATM* and ICI outcomes, including *KRAS, TP53, KEAP1,* and *STK11* (Materials and Methods). In these models, *TP53* and *KEAP1* status associated positively and negatively with ICI-mono outcomes, respectively, whereas *ATM* associated with outcome only to ICI-chemo, along with *STK11*, *KEAP1*, and *KRAS* (Supplementary Fig. S6B). Concordantly, outcomes in patients with *ATM* mutations treated with ICI-chemo trended toward improvement compared with those with ICI-mono, suggesting preferential benefit to the addition of chemotherapy to ICI in patients with *ATM* mutations (Supplementary Fig. S7A and S7B).

To further interrogate the putative functionality of *ATM* mutations and how they associate with outcome, we repeated the above analyses, now comparing truncating mutations with all missense mutations versus wild-type *ATM* (Supplementary Fig. S8). As expected, tumors with *ATM* missense mutations had the highest TMB, with similar PD-L1 distributions (Supplementary Fig. S8A and S8B). In the outcome analysis, after multivariate adjustment, neither truncating nor missense *ATM* mutations associated with OS to ICI-mono nor Chemo-mono; however, despite the decreased power in this subgroup analysis, truncating ATM mutations had a borderline significant association with OS to ICI-chemo [HR, 0.731; 95% confidence interval (CI), 0.899–1.038; $P = 0.080$], consistent with the hypothesis that functional *ATM* loss is driving the observed outcome association and that truncating mutations have a more consistent functional effects than *ATM* missense mutations (Supplementary Fig. S8C and S8D).

ATM loss associates with increased activation of STING signaling with chemotherapy

Prior experimental work has demonstrated an association between ATM inhibition and STING activity (11–13), which may represent a possible mechanism linking *ATM* loss and ICI outcomes. To better understand how genomic *ATM* loss affects immune activation and validate the above clinical findings, we evaluated STING signaling in *ATM*-deficient preclinical models. We generated isogenic *ATM* knock-out (KA) cells using CRISPR/Cas9 technology in a *Kras* mutant murine primary cell line (LKR13 K). Protein expression assessed by western blotting revealed a modest upregulation of cGAS and total STING levels in KA when compared with K control cells, although it did not reach statistical significance (**Fig. 5A** and **B**; Supplementary Fig. S9). However, *ATM* loss had no impact on total or phosphorylated IFN regulatory factor 3 (phospho-IRF3), a downstream target of

STING signaling responsible for the transcription of multiple immune genes, including type-I IFN (ref. 46; **Fig. 5A** and **B**; Supplementary Fig. S9A).

To further characterize STING signaling in ATM-deficient tumor cells, we evaluated expression of downstream immune-stimulatory factors and pro-inflammatory cytokines, specifically IFNα, a type-I IFN induced by IRF3 (47), and CXCL10, a proinflammatory cytokine induced by type-I IFN after STING activation (48). Although basal levels of IFNα expression were no different in ATM-proficient versus deficient cells (**Fig. 5C**), CXCL10 secretion was significantly lower (K vs. KA, 23.21 vs. 5.22 pg/mL; $P = 0.0009$; **Fig. 5D**). Taken together, these results suggest that, although *ATM* loss associates with increased cGAS and STING activation, it does not translate to increased downstream activity and in fact associated with decreased cytokine expression, consistent with dysfunctional activation of STING signaling and possible impaired antitumor immune response.

To determine whether chemotherapy modulated the effect of *ATM* loss on STING signaling, we then evaluated STING pathway and downstream cytokine expression after treatment with different chemotherapies using our murine cell lines (K and KA) and additional *ATM*-wt (H2030) and *ATM*-mt (H23) human cell lines. In the *ATM* intact cells (K), chemotherapy either had no effect (cisplatin, gemcitabine, and pemetrexed) or led to decreased expression (docetaxel, topotecan, and SN-38) of cGAS, STING, and downstream targets phopho-TBK1 and phospho-IRF3 (**Fig. 5E** and **F**). Conversely, *ATM*-deficient cells (KA) showed an upregulation of cGAS, STING, phospho-TBK1, and phospho-IRF3 proteins when treated with all chemotherapies compared with untreated K and KA cells, although it was most robust for docetaxel, topotecan, and SN-38 chemotherapies (**Fig. 5E** and **F**). Concordantly, when we assessed CXCL10 induction after chemotherapy treatments, KA cells demonstrated stronger relative induction than *ATM*-proficient K cells for all chemotherapies, although only pemetrexed, docetaxel, and SN-38 reached statistical significance. By contrast, only pemetrexed significantly induced CXCL10 secretion in K cells (**Fig. 5G**), whereas topotecan and SN-38 actually decreased CXCL10 secretion in *ATM*-proficient cells (**Fig. 5G**; Supplementary Fig. S9B). As a control, we also assessed overall sensitivity to these different chemotherapies, and observed that *ATM* loss did not alter sensitivity to cisplatin, gemcitabine, or docetaxel. Conversely, lack of ATM expression significantly increased IC_{50} value for pemetrexed, topotecan or SN-38 chemotherapies (Supplementary Fig. S9C). Evaluation of STING signaling activation after chemotherapy treatments assessed in human cell lines further support these findings. Chemotherapy treatments showed minimal or no effects on STING signaling activation in H2030 cell line (*ATM*-wt), whereas all chemotherapies, particularly docetaxel, topotecan and SN-38, induced a strong upregulation of STING signaling proteins in H23 cells (*ATM*-mt; Supplementary Fig. S10A and S10B).

Discussion

In this large, retrospective genomic analysis, we show that *ATM* mutations in NSCLC have specific patterns of co-mutational enrichment and exclusivity, frequently co-occurring with *KRAS* mutations and often mutually exclusive with *EGFR* mutations. We note that *KRAS* co-mutation status further constrains the co-mutation landscape, with enhanced mutual exclusivity with *TP53* and *KEAP1* in this context. Finally, in a large, real-world clinical cohort, we observed an association between *ATM* loss and benefit specifically to ICI given with chemotherapy, but not ICI-monotherapy, which was corroborated *in vitro* by increased STING signaling after treatment with chemotherapy.
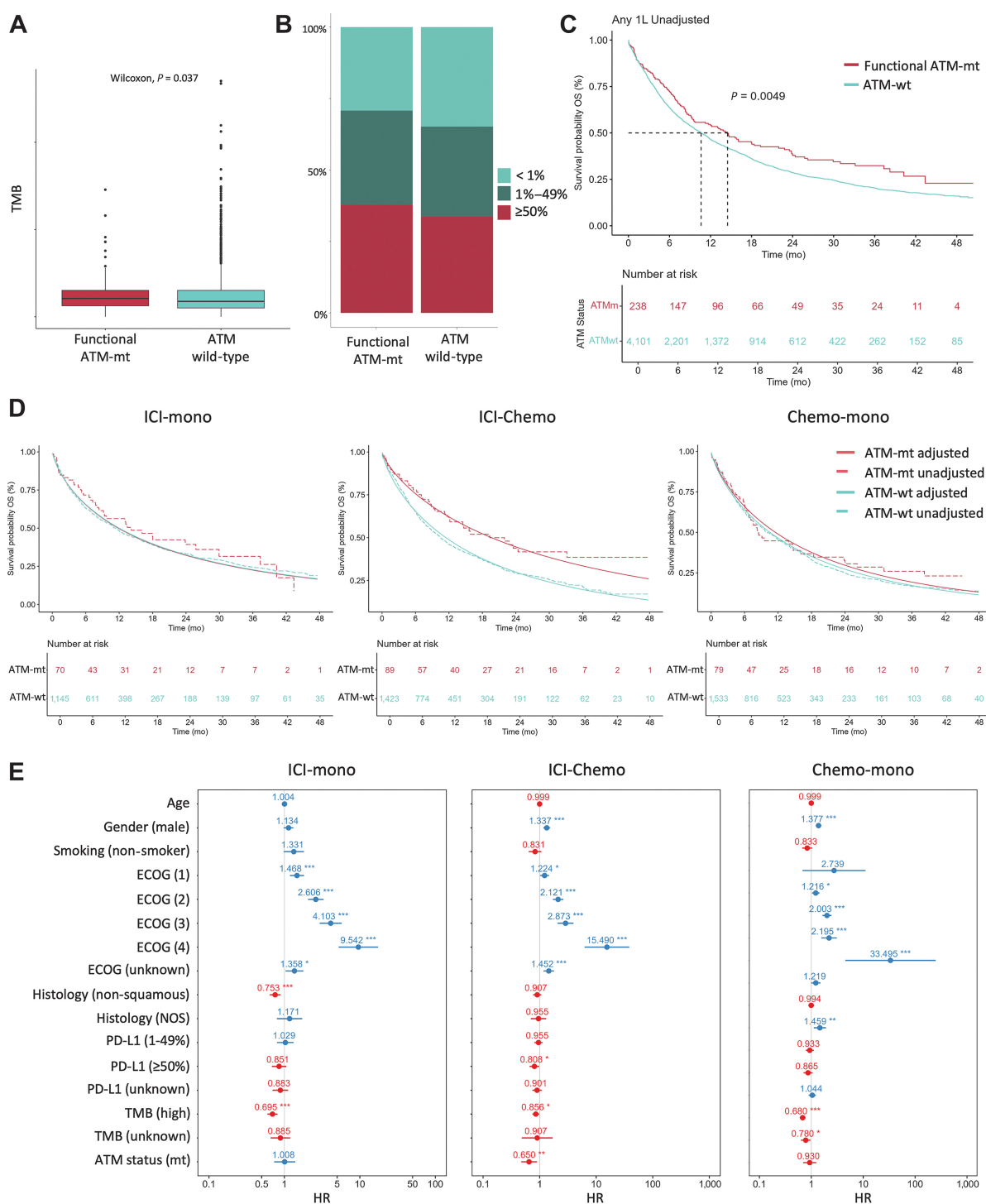
Figure 4.
Association between ATM and immune checkpoint inhibitor (ICI) outcomes. **A,** Tumor mutational burden (TMB) in patients with functional *ATM* mutations (*ATM*-mt) versus wild-type (*ATM*-wt) samples in the FH-FMI CGDB Clinical Cohort. *ATM* mutations defined as truncating, splice site, or select curated mutations. **B,** PD-L1 expression in *ATM*-mt versus *ATM*-wt samples. **C,** Overall survival (OS) in *ATM*-mt versus *ATM*-wt samples across the entire FH-FMI CGDB clinical cohort. **D,** OS in *ATM*-mt versus *ATM*-wt samples, stratified by treatment with ICI-monotherapy (ICI-mono), ICI with chemotherapy (ICI-chemo), or chemotherapy monotherapy (Chemo-mono). Dashed lines represent unadjusted values and solid lines represent multivariable adjustment. **E,** Forest plot for multivariable analysis of clinical features, ATM status, and OS, stratified by treatment. Points represent hazard ratio and lines 95% confidence interval. Red values indicate an association with improved outcome (HR < 1), blue with a negative outcome (HR > 1), and stars are placed next to statistically significant *P* values. *, *P* < 0.05; **, *P* < 0.01; ***, *P* < 0.001.
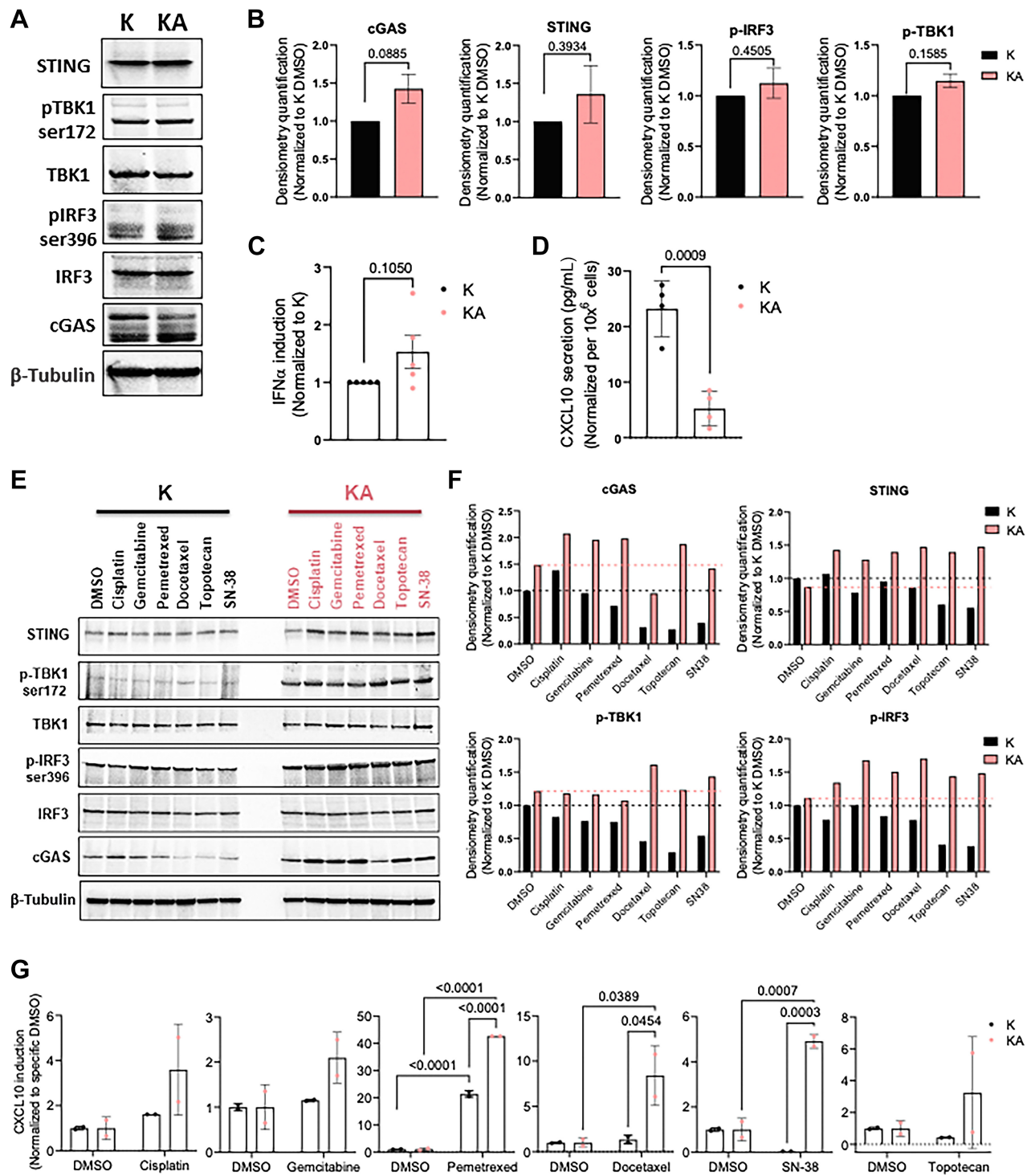
Figure 5.
ATM loss enhances STING signaling activation with chemotherapy. **A,** Western blot analysis and (**B**) quantification of expression of the indicated STING signaling proteins in *ATM*-proficient (K) and *ATM*-deficient (KA) cells. Graphs show average of 2–3 independent Western blots. α-Tubulin was used as a loading control. **C,** Quantification of IFNα mRNA expression assessed by RT-PCR in K and KA cell lines. **D,** ELISA quantification of CXCL10 protein secretion in K and KA cell lines normalized by 10^6 cells. **E,** Western blot analysis and (**F**) quantification of expression of the indicated STING signaling proteins in *ATM*–proficient K and *ATM*-deficient (KA) cells after DMSO, 10 μmol/L cisplatin, 40 nmol/L gemcitabine, 50 nmol/L pemetrexed, 500 nmol/L docetaxel, 400 nmol/L topotecan or 300 nmol/L SN-38 treatments for 48 hours. α-Tubulin was used as a loading control. **G,** ELISA quantification of CXCL10 protein secretion normalized by 10^6 cells in K and KA cell lines after DMSO, 10 μmol/L cisplatin, 40 nmol/L gemcitabine, 50 nmol/L pemetrexed, 500 nmol/L docetaxel, 400 nmol/L topotecan or 300 nmol/L SN-38 treatments for 48 hours. Graphs show relative induction normalized to DMSO non-treated K or KA cells, respectively. All data are presented as mean ± standard error of the mean (error bars) for each group.

The pattern of mutual exclusivity between *ATM* and other lung cancer genes, specifically *TP53*, *KEAP1*, and *EGFR*, raises important questions about possible dependencies on these pathways in the context of *ATM* loss. In particular, we observed that *ATM* and *TP53* mutations are largely mutually exclusive in *KRAS*-mutated tumors, and that the *ATM* mutations that do co-occur with *TP53* are more likely to be missense mutations in high TMB tumors, suggesting that these may be non-functional passenger mutations. This is concordant with a recent report that showed that tumors with absent ATM protein expression were less likely to have *TP53* mutations (45), and is also consistent with previous work showing that combined *TP53* and *ATM* loss is statistically underrepresented in human tumors (49). Although the mechanism behind this mutual exclusivity needs further study, preclinical data suggest a possible synthetic lethal relationship, particularly in the context of *KRAS* mutations; in murine models, inactivation of *Atm* was tolerated in a P53-proficient context, but was incompatible with cellular viability in the context of oncogenically activated *Kras* and bilallelic *Tp53* inactivation (50), possibly due to decreased tolerance of genotoxic stress. Whether *EGFR* and *KEAP1* are also mutually exclusive to *ATM* due to decreased tolerance of *ATM* loss, or because *ATM* is redundant in these contexts, will require further study. However, these patterns suggest possible genomic contexts in which ATM inhibition may be particularly effective (49) and warrant further clinical investigation.

One barrier to the study of *ATM*-mutated NSCLC has been limited data as to the functional effects of most *ATM* alterations. To-date, a small group of studies has shown associations between specific *ATM* mutations and decreased protein expression (9, 10, 51), but only a limited set of mutations has been assayed, and no full mutagenic/functional screen has been carried out. Our data confirm that truncating events associate with decreased protein expression and likely drive the observed outcome association, whereas the functional status of missense ATM mutations, especially those without prior annotation, should be treated with caution. Our data further suggest that co-mutation status may provide further contextual clues, as co-mutation with *KRAS* was enriched for likely functional mutations, compared with likely mutual exclusivity with *TP53* and *EGFR* as discussed. If therapeutic strategies in *ATM* mutant tumors continue to develop, direct assessment via IHC may be a promising strategy (10). However, these data also point to the need for further studies that more conclusively classify the effect of *ATM* mutations not just on protein expression but on protein function, and highlight the need for caution in assuming that any *ATM* event, especially a missense mutation, is functionally significant.

Finally, our data provide important context to previous reports associating *ATM* with ICI outcomes. In particular, after adjustment for clinicogenomic features, we found no association between *ATM* mutations and ICI-monotherapy outcomes, and the above discussion suggests that the previously published association between *ATM/TP53* co-mutations and ICI benefit (14) may be driven by the confounding association between TMB and ICI response rather than a more specific functional effect from *ATM* loss. However, we newly demonstrate that *ATM* mutations do appear to exert a modest effect on ICI outcomes given with chemotherapy. This finding builds on a recent publication that demonstrated a non-significant trend toward improved outcomes in ICI-chemo–treated patients, consistent the modest effect we observed but likely underpowered in their smaller cohort (45). Although our data did not identify any association between *ATM* loss and known mutational signatures to drive the ICI association, our *in vitro* data suggest that chemotherapy in the context of *ATM* loss can enhance STING signaling. Prior work has shown that DNA damage

can activate IFN signaling through the STING pathway (11, 52, 53), suggesting a possible mechanism for how DNA-damaging chemotherapies in the context of impaired ATM activity can enhance this phenotype. Interestingly, in contrast with our data, prior work has shown increased STING activity after ATM inhibition even without chemotherapy (11–13). However, these prior studies did not completely assess the STING pathway in the context of genomic *ATM* loss, and most relied on ATM inhibitors, which may have different effects on cytokine production than genomic *ATM* loss (54). More work will be necessary to further define the mechanism underlying this association and validate a specific vulnerability to ICI-chemotherapy or ICI in combination with other DDR inhibitors.

This study has several limitations, including the retrospective nature of our cohorts and imperfect clinical annotations from the real-world cohort, though similar outcome analyses from this database have been performed (55). In addition, as discussed, analyses of *ATM* mutations are limited by incomplete functional annotations; however, we believe that our analysis may offer some insight on this question, and we attempted to mitigate these effects on the clinical outcome analysis by applying more stringent selection criteria that are concordant with prior publications and multiple ongoing clinical studies (Clinical-Trials.gov Identifier: NCT03334617). Finally, we note that validation in isogenic human cell lines was beyond the scope of the current analysis, and the human cell line data presented may be confounded by other genomic differences between the tested cell lines.

In sum, we believe this is the largest and most complete analysis to-date of the landscape of *ATM* mutations in NSCLC and their therapeutic implications. Our work highlights the importance of considering mutation type and co-mutation status in assessing *ATM* mutation functionality, suggests that *ATM* mutations associate with response to ICI-chemotherapy but not monotherapy, and is hypothesis-generating for potential therapeutic strategies in *ATM* mutant tumors as well as the application of ATM inhibitors in vulnerable genotypes.

Authors' Disclosures

Authors' Contributions

N.I. Vokes: Conceptualization, resources, data curation, formal analysis, super-vision, investigation, writing–original draft, writing–review and editing. **A. Galan Cobo:** Conceptualization, resources, formal analysis, supervision, investigation, methodology, writing–original draft. **M. Fernandez-Chas:** Data curation, software, formal analysis, investigation. **D. Molkentine:** Investigation, visualization, method-ology, writing–original draft. **S. Treviño III:** Data curation, formal analysis, inves-tigation, visualization. **V. Druker:** Data curation, formal analysis, supervision, investigation, visualization. **Y. Qian:** Investigation, visualization, methodology. **S. Patel:** Investigation, visualization, methodology. **S. Schmidt:** Data curation. **L. Hong:** Resources, data curation, formal analysis. **J. Lewis:** Data curation. **W. Rinsurongkawong:** Data curation. **V. Rinsurongkawong:** Data curation. **J.J. Lee:** Data curation. **M.V. Negrao:** Data curation. **D.L. Gibbons:** Resources, data curation, investigation. **A. Vaporciyan:** Resources, data curation. **X. Le:** Conceptualization, resources, data curation. **J. Wu:** Conceptualization, formal analysis. **J. Zhang:** Conceptualization, resources, data curation. **U. Rigney:** Conceptualization, resources, data curation, formal analysis. **S. Iyer:** Conceptualization, resources, data curation, formal analysis. **E. Dean:** Conceptualization, resources, data curation, formal analysis.

J.V. Heymach: Conceptualization, resources, data curation, formal analysis, super-vision, funding acquisition, investigation, visualization, writing–original draft, project administration, writing–review and editing.

Acknowledgments

Note

References

1. Lavin MF. Ataxia-telangiectasia: from a rare disorder to a paradigm for cell signalling and cancer. Nat Rev Mol Cell Biol 2008;9:759–69.

2. Derheimer FA, Kastan MB. Multiple roles of ATM in monitoring and main-taining DNA integrity. FEBS Lett 2010;584:3675–81.

3. Taylor AMR, Harnden DG, Arlett CF, Harcourt SA, Lehmann AR, Stevens S, et al. Ataxia telangiectasia: a human mutation with abnormal radiation sensi-tivity. Nature 1975;258:427–9.

4. Lavin MF, Shiloh Y. The genetic defect in ataxia-telangiectasia. Annu Rev Immunol 1997;15:177–202.

5. The Cancer Genome Atlas Research Network. Comprehensive molecular pro-filing of lung adenocarcinoma. Nature 2014;511:543–50.

6. The Cancer Genome Atlas Research Network. Comprehensive genomic char-acterization of squamous cell lung cancers. Nature 2012;489:519–25.

7. Villaruz LC, Jones H, Dacic S, Abberbock S, Kurland BF, Stabile LP, et al. ATM protein is deficient in over 40% of lung adenocarcinomas. Oncotarget 2016;7: 57714–25.

8. Petersen LF, Klimowicz AC, Otsuka S, Elegbede AA, Petrillo SK, Williamson T, et al. Loss of tumour-specific ATM protein expression is an independent prognostic factor in early resected NSCLC. Oncotarget 2017;8:38326–36.

9. Mitui M, Nahas SA, Du LT, Yang Z, Lai CH, Nakamura K, et al. Functional and computational assessment of missense variants in the ataxia-telangiectasia mutated (ATM) gene: mutations with increased cancer risk. Hum Mutat 2009;30:12–21.

10. Weber AM, Drobnitzky N, Devery AM, Bokobza SM, Adams RA, Maughan TS, et al. Phenotypic consequences of somatic mutations in the ataxia-telangiectasia mutated gene in non–small cell lung cancer. Oncotarget 2016;7:60807–22.

11. Härtlova A, Erttmann SF, Raffi FA, Schmalz AM, Resch U, Anugula S, et al. DNA damage primes the Type I interferon system via the cytosolic DNA sensor STING to promote anti-microbial innate immunity. Immunity 2015;42:332–43.

12. Zhang Q, Green MD, Lang X, Lazarus J, Parsels JD, Wei S, et al. Inhibition of ATM increases interferon signaling and sensitizes pancreatic cancer to immune checkpoint blockade therapy. Cancer Res 2019;79:3940–51.

13. Hu M, Zhou M, Bao X, Pan D, Jiao M, Liu X, et al. ATM inhibition enhances cancer immunotherapy by promoting mtDNA leakage and cGAS/STING activation. J Clin Invest 2021;131:e139333.

14. Chen Y, Chen G, Li J, Huang Y-Y, Li Y, Lin J, et al. Association of tumor protein p53 and ataxia-telangiectasia mutated comutation with response to immune

15. checkpoint inhibitors and mortality in patients with non–small cell lung cancer. JAMA Netw Open 2019;2:e1911895.

15. Ricciuti B, Recondo G, Spurr LF, Li YY, Lamberti G, Venkatraman D, et al. Impact of DNA damage response and repair (DDR) gene mutations on efficacy of PD-(L)1 immune checkpoint inhibition in non–small cell lung cancer. Clin Cancer Res 2020;26:4135–42.

16. Ravi A, Hellmann MD, Arniella MB, Holton M, Freeman SS, Naranbhai V, et al. Genomic and transcriptomic analysis of checkpoint blockade response in advanced non–small cell lung cancer. Nat Genet 2023;55:807–19.

17. Cheng B, Pan W, Xing Y, Xiao Y, Chen J, Xu Z. Recent advances in DDR (DNA damage response) inhibitors for cancer therapy. Eur J Med Chem 2022;230: 114109.

18. AACR Project GENIE Consortium. AACR project GENIE: powering precision medicine through an international consortium. Cancer Discov 2017;7:818–31.

19. Nguyen B, Fong C, Luthra A, Smith SA, DiNatale RG, Nandakumar S, et al. Genomic characterization of metastatic patterns from prospective clinical sequencing of 25,000 patients. Cell 2022;185:563–75.

20. Campbell JD, Alexandrov A, Kim J, Wala J, Berger AH, Pedamallu CS, et al. Distinct patterns of somatic genome alterations in lung adenocarcinomas and squamous cell carcinomas. Nat Genet 2016;48:607–16.

21. Cerami E, Gao J, Dogrusoz U, Gross BE, Sumer SO, Aksoy BA, et al. The cBio cancer genomics portal: an open platform for exploring multidimensional cancer genomics data. Cancer Discov 2012;2:401–4.

22. Gao J, Aksoy BA, Dogrusoz U, Dresdner G, Gross B, Sumer SO, et al. Integrative analysis of complex cancer genomics and clinical profiles using the cBioPortal. Sci Signal 2013;6:pl1.

23. Mitchell KG, Diao L, Karpinets T, Negrao MV, Tran HT, Parra ER, et al. Neutrophil expansion defines an immunoinhibitory peripheral and intratumoral inflammatory milieu in resected non–small cell lung cancer: a descriptive analysis of a prospectively immunoprofiled cohort. J Immunother Cancer 2020;8:e000405.

24. Schmidt ST, Akhave N, Knightly RE, Reuben A, Vokes N, Zhang J, et al. Shared nearest neighbors approach and interactive browser for network analysis of a comprehensive non–small cell lung cancer data set. JCO Clin Cancer Inform 2022;6:e2200040.

25. Federico L, McGrail DJ, Bentebibel S-E, Haymaker C, Ravelli A, Forget M-A, et al. Distinct tumor-infiltrating lymphocyte landscapes are associated with

clinical outcomes in localized non–small cell lung cancer. Ann Oncol 2022;33: 42–56.

26. Singal G, Miller PG, Agarwala V, Li G, Kaushik G, Backenroth D, et al. Association of patient characteristics and tumor genomics with clinical outcomes among patients with non–small cell lung cancer using a clinicogenomic database. JAMA 2019;321:1391–9.

27. Garcia EP, Minkovsky A, Jia Y, Ducar MD, Shivdasani P, Gong X, et al. Validation of OncoPanel: a targeted next-generation sequencing assay for the detection of somatic variants in cancer. Arch Pathol Lab Med 2017;141:751–8.

28. Cheng DT, Mitchell TN, Zehir A, Shah RH, Benayed R, Syed A, et al. Memorial sloan kettering-integrated mutation profiling of actionable cancer targets (MSK-IMPACT). J Mol Diagn JMD 2015;17:251–64.

29. Le X, Puri S, Negrao MV, Nilsson MB, Robichaux J, Boyle T, et al. Landscape of EGFR-dependent and -independent resistance mechanisms to osimertinib and continuation therapy beyond progression in EGFR-mutant NSCLC. Clin Cancer Res 2018;24:6195–203.

30. Robichaux JP, Le X, Vijayan RSK, Hicks JK, Heeke S, Elamin YY, et al. Structure-based classification predicts drug response in EGFR-mutant NSCLC. Nature 2021;597:732–7.

31. Parra ER, Uraoka N, Jiang M, Cook P, Gibbons D, Forget M-A, et al. Validation of multiplex immunofluorescence panels using multispectral microscopy for immune-profiling of formalin-fixed and paraffin-embedded human tumor tissues. Sci Rep. 2017;7:13380.

32. Gaudreau P-O, Negrao MV, Mitchell KG, Reuben A, Corsini EM, Li J, et al. Neoadjuvant chemotherapy increases cytotoxic T-cell, tissue resident memory T-cell, and B-cell infiltration in resectable NSCLC. J Thorac Oncol 2021; 16:127–39.

33. Reuben A, Zhang J, Chiou S-H, Gittelman RM, Li J, Lee W-C, et al. Comprehensive T-cell repertoire characterization of non–small cell lung cancer. Nat Commun 2020;11:603.

34. Frampton GM, Fichtenholtz A, Otto GA, Wang K, Downing SR, He J, et al. Development and validation of a clinical cancer genomic profiling test based on massively parallel DNA sequencing. Nat Biotechnol 2013;31:1023–31.

35. Woodhouse R, Li M, Hughes J, Delfosse D, Skoletsky J, Ma P, et al. Clinical and analytical validation of FoundationOne Liquid CDx, a novel 324-Gene cfDNA-based comprehensive genomic profiling assay for cancers of solid tumor origin. PLoS ONE 2020;15:e0237802.

36. He J, Abdel-Wahab O, Nahas MK, Wang K, Rampal RK, Intlekofer AM, et al. Integrated genomic DNA/RNA profiling of hematologic malignancies in the clinical setting. Blood 2016;127:3004–14.

37. Vokes NI, Liu D, Ricciuti B, Jimenez-Aguilar E, Rizvi H, Dietlein F, et al. Harmonization of tumor mutational burden quantification and association with response to immune checkpoint blockade in non–small cell lung cancer. JCO Precis Oncol 2019;3:PO.19.00171.

38. Chalmers ZR, Connelly CF, Fabrizio D, Gay L, Ali SM, Ennis R, et al. Analysis of 100,000 human cancer genomes reveals the landscape of tumor mutational burden. Genome Med 2017;9:34.

39. Rosenthal R, McGranahan N, Herrero J, Taylor BS, Swanton C. deconstructSigs: delineating mutational processes in single tumors distinguishes DNA repair deficiencies and patterns of carcinoma evolution. Genome Biol 2016;17:31.

40. Wislez M, Spencer ML, Izzo JG, Juroske DM, Balhara K, Cody DD, et al. Inhibition of mammalian target of rapamycin reverses alveolar epithelial neoplasia induced by oncogenic K-ras. Cancer Res 2005;65:3226–35.

41. Ricciuti B, Wang X, Alessi JV, Rizvi H, Mahadevan NR, Li YY, et al. Association of high tumor mutation burden in non–small cell lung cancers with increased immune infiltration and improved clinical outcomes of PD-L1 blockade across PD-L1 expression levels. JAMA Oncol 2022;8:1160–8.

42. Skoulidis F, Byers LA, Diao L, Papadimitrakopoulou VA, Tong P, Izzo J, et al. Co-occurring genomic alterations define major subsets of KRAS-mutant lung adenocarcinoma with distinct biology, immune profiles, and therapeutic vulnerabilities. Cancer Discov 2015;5:860–77.

43. Scheffler M, Ihle MA, Hein R, Merkelbach-Bruse S, Scheel AH, Siemanowski J, et al. K-ras mutation subtypes in NSCLC and associated co-occuring mutations in other oncogenic pathways. J Thorac Oncol 2019;14:606–16.

44. Arbour KC, Jordan E, Kim HR, Dienstag J, Yu HA, Sanchez-Vega F, et al. Effects of co-occurring genomic alterations on outcomes in patients with KRAS-mutant non–small cell lung cancer. Clin Cancer Res 2018;24:334–40.

45. Ricciuti B, Elkrief A, Alessi J, Wang X, Li Y, Gupta H, et al. Clinicopathologic, genomic, and immunophenotypic landscape of ATM mutations in non–small cell lung cancer. Clin Cancer Res 2023;OF1–11.

46. Abe T, Harashima A, Xia T, Konno H, Konno K, Morales A, et al. STING recognition of cytoplasmic DNA instigates cellular defense. Mol Cell 2013;50: 5–15.

47. Sun L, Wu J, Du F, Chen X, Chen ZJ. Cyclic GMP–AMP synthase is a cytosolic DNA sensor that activates the Type I interferon pathway. Science 2013;339:786–91.

48. Cañadas I, Thummalapalli R, Kim JW, Kitajima S, Jenkins RW, Christensen CL, et al. Tumor innate immunity primed by specific interferon-stimulated endogenous retroviruses. Nat Med 2018;24:1143–50.

49. Jiang H, Reinhardt HC, Bartkova J, Tommiska J, Blomqvist C, Nevanlinna H, et al. The combined status of ATM and p53 link tumor development with therapeutic response. Genes Dev 2009;23:1895–909.

50. Schmitt A, Knittel G, Welcker D, Yang T-P, George J, Nowak M, et al. ATM deficiency is associated with sensitivity to PARP1- and ATR inhibitors in lung adenocarcinoma. Cancer Res 2017;77:3040–56.

51. Huang K, Mashl RJ, Wu Y, Ritter DI, Wang J, Oh C, et al. Pathogenic germline variants in 10,389 adult cancers. Cell 2018;173:355–70.

52. Sen T, Rodriguez BL, Chen L, Corte CMD, Morikawa N, Fujimoto J, et al. Targeting DNA damage response promotes antitumor immunity through STING-mediated T-cell activation in small-cell lung cancer. Cancer Discov 2019;9:646–61.

53. Ahn J, Xia T, Konno H, Konno K, Ruiz P, Barber GN. Inflammation-driven carcinogenesis is mediated through STING. Nat Commun 2014;5:5166.

54. Menolfi D, Zha S. ATM, ATR and DNA-PKcs kinases—the lessons from the mouse models: inhibition ≠ deletion. Cell Biosci 2020;10:8.

55. Pérol M, Felip E, Dafni U, Polito L, Pal N, Tsourti Z, et al. Effectiveness of PD-(L)1 inhibitors alone or in combination with platinum-doublet chemotherapy in first-line (1L) non-squamous non–small cell lung cancer (nsq-NSCLC) with PD-L1–high expression using real-world data. Ann Oncol 2022;33:511–21.